CASL-¦-2013-0346-000

Power uprates
and plant life extension

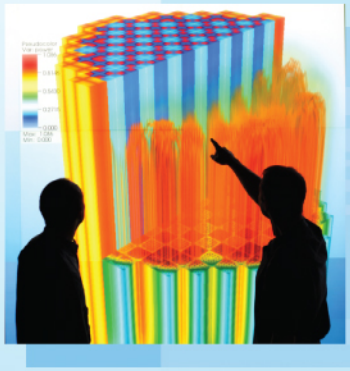

Engineering design
and analysis

Science-enabling
high performance
computing

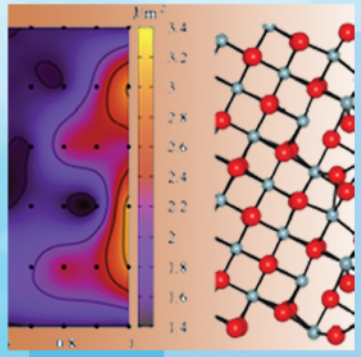

Fundamental science

Plant operational data

Consortium for Advanced Simulation of LWRs

Demonstration of Hyrax Capabilities

A.M. Jokisaari and K. Thornton
University of Michigan

March 29, 2013

U.S. DEPARTMENT OF ENERGY | Nuclear Energy

CASL-MPO Deliverable: Demonstration of Hyrax Capabilities

A. M. Jokisaari, K. Thornton

March 29, 2013

L3:MPO.CORROSION.P6.01

1 Introduction

The formation of zirconium hydrides in zirconium alloys is an important aspect of the microstructural evolution of fuel-pin cladding materials in light water reactors. To maximize fuel performance and lifetime, a more in-depth understanding and a predictive model of hydrogen effects on the cladding is required than is currently used in fuel performance codes. A phase field modeling framework, Hyrax, has been developed to examine the precipitation and growth of zirconium hydrides within zirconium, using the finite element framework MOOSE (Multiphysics Object Oriented Simulation Environment [1]), developed at Idaho National Laboratory. Hyrax incorporates into a phase field model a nucleation algorithm based on classical nucleation theory [2, 3], heat conduction, and hydride/zirconium misfit strain [4, 5] to examine precipitation and growth phenomena in single crystal zirconium. The framework aims to elucidate how macroscopic agglomerates of aligned microscopic hydride arrays form [6, 7, 8, 9] and why there exists a hysteresis in the terminal solid solubility of hydrogen in zirconium between dissolution and precipitation [10]. We have conducted extensive testing for code validation and we include examples that demonstrate Hyrax capabilities. Finally, near-future plans are discussed, including parameterization for δ-hydrides and the inclusion of temperature dependence into the model.

2 Computational approach based on MOOSE

MOOSE was chosen as the framework on which to build Hyrax for several reasons. MOOSE is an easily extendable, fully coupled multiphysics finite element framework. It has a modular design, so that partial differential equations, boundary conditions, initial conditions, material properties, and other tools can be activated in a simulation by adding corresponding blocks in an input file. The structure of MOOSE is schematically illustrated within the red center box of Fig. 1. MOOSE is dimensionally agnostic and parallelization occurs in the MOOSE backend. Therefore, the application code does not require re-compiling

for different dimensionalities, and it is designed to be computationally efficient on both laptops and high-performance environments. MOOSE has a large user base and a dedicated developer team, and general-use code can be contributed into a shared library (Extended Library of Kernels, ELK) for reuse and adaptation by the community. MOOSE uses libMesh [11] as its meshing library, which is also under active development. LibMesh supports mesh adaptivity, which is useful for large-scale phase field simulations. It should be noted that many other CASL activities involve MOOSE-based applications for a wide range of simulations, and therefore provides a path for easier integration of codes in the future.

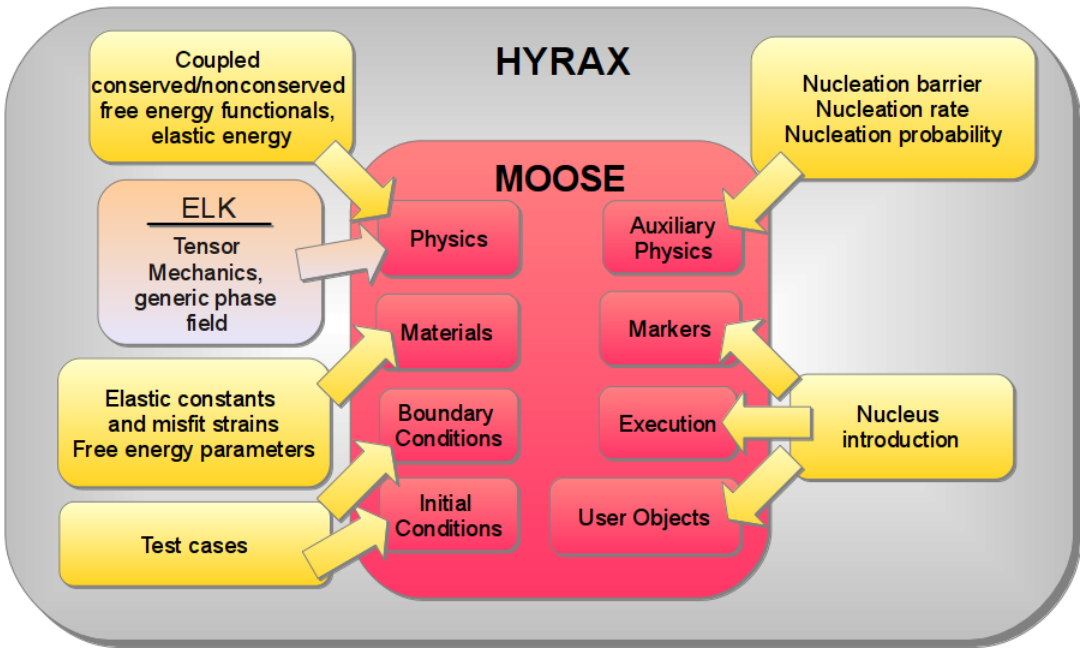

Figure 1: Schematic illustration of the Hyrax application (gray outer box) over the MOOSE framework (red center box). The Hyrax application is built upon the MOOSE partial differential equation solver framework and the ELK extended library (orange box). MOOSE consists of physics (partial differential equations), auxiliary physics, materials (constitutive equations and material constants), boundary conditions, initial conditions, mesh markers, user objects, custom execution and postprocessors (not shown). Hyrax implements the coupled Cahn-Hilliard and Allen-Cahn equations and an elasticity solver in the physics as well as appropriate boundary conditions (yellow boxes). Any spatially dependent or independent material properties of the system, such as thermal conductivity or elastic stiffness, are implemented into the materials system. The auxiliary system ("auxiliary physics") solves for any additional field variables that are not part of a partial differential equation, such as nucleation rate. Nucleation events are explicitly introduced into the phase field simulation using the mesh element marker system, a special transient executioner, and the general-purpose user object system.

3 Hyrax Structure

For a solid-solid transformation such as the zirconium to zirconium hydride transformation, the free energy is composed of bulk (F_{bulk}), gradient (F_{grad}), and strain (F_{strain}) terms,

as

$$F = F_{bulk} + F_{grad} + F_{strain}. \tag{1}$$

The bulk contribution is related to the chemical potential due to compositional inhomogeneities, the gradient term is related to the interfacial energy between phases, and the strain energy may generally involve both elastic and plastic strain, originating from the presence of long-range strain fields due to the misfit between different phases, composition gradients, or dislocations. In this particular case, we include only the elastic contribution to the strain energy, giving $F_{strain} = F_{elastic}$.

The zirconium-zirconium hydride system is described using a conserved field variable, χ, that tracks the concentration of hydrogen, and a non-conserved structural field variable, ϕ, that tracks the lattice transformation between the two phases. Because the hcp-zirconium unit cell has 120 degree rotational symmetry around the c-axis, there are three orientations of hydrides with respect to the zirconium matrix that are energetically equivalent; these variants are tracked by three field variables, ϕ_1, ϕ_2, and ϕ_3, in a manner similar to Ref. [12].

In terms of these field variables, the free energy given in Eq. 1 is expressed as

$$F = \int_V \left(f\left(\chi, \phi_1, \phi_2, \phi_3\right) + \sum_{h=1}^{3} \frac{\kappa_h}{2} |\nabla \phi_h\left(\mathbf{r}\right)|^2 + \frac{\kappa_\chi}{2} |\nabla \chi\left(\mathbf{r}\right)|^2 \right) dV + F_{elastic} \tag{2}$$

where $f\left(\chi, \phi_1, \phi_2, \phi_3\right)$ is the bulk chemical free energy, κ indicates a gradient energy coefficient, and $F_{elastic}$ is given as

$$F_{elastic} = \int_V \left(\frac{1}{2} C_{ijkl} \left(\tilde{\epsilon}_{ij}\left(\mathbf{r}\right) - \sum_h \epsilon_{ij}^{0h} \phi_h^2\left(\mathbf{r}\right) \right) \left(\tilde{\epsilon}_{kl}\left(r\right) - \sum_h \epsilon_{kl}^{0h} \phi_h^2\left(\mathbf{r}\right) \right) \right) dV. \tag{3}$$

Here, C_{ijkl} is the stiffness tensor, $\tilde{\epsilon}_{ij}$ indicates the local strain, and ϵ_{ij}^{0h} indicates the hydride-zirconium misfit strain for the hth orientation variant (see Refs. [4, 12]). The bulk chemical free energy functional used in the phase field model is currently defined following Ref. [12], which is for a system of hcp zirconium and γ-hydrides due to the lack of data for δ-hydrides in the literature. The bulk chemical free energy for zirconium and δ-hydrides is currently under development in Van der Ven's group. However, data exist in the literature for the misfit strains for both γ-hydrides [12] and δ-hydrides [5].

3.1 Evolution equations and their implementation

The Cahn-Hilliard equation governs the evolution of the concentration of hydrogen in the system as

$$\frac{\partial \chi\left(\mathbf{r}, t\right)}{\partial t} = \nabla \cdot \left[M \nabla \left(\frac{\partial f}{\partial \chi} - \kappa_\chi \nabla^2 \chi + \frac{\delta F_{elastic}}{\delta \chi} \right) \right] \tag{4}$$

and the Allen-Cahn equation governs the evolution of the nonconserved phase order parameters as

$$\frac{\partial \phi_h(\mathbf{r},t)}{\partial t} = -L_h\left(\frac{\partial f}{\partial \phi_h} - \kappa_h \nabla^2 \phi_h + \frac{\delta F_{elastic}}{\delta \phi_h}\right) \tag{5}$$

where there are h number of Allen-Cahn equations, one for each structural order parameter. The mobility M and the kinetic coefficient L can be anisotropic and are currently parameterized following Ref. [12].

"Kernels" handle portions of the partial differential equations governing the simulation. They operate on a single variable, but can couple with other variables and material properties. Three separate kernel classes have been written for Hyrax to calculate $\frac{\partial f}{\partial \chi}$, $\frac{\partial f}{\partial \phi_h}$, and $\frac{\delta F_{elastic}}{\delta \phi_h}$, which can be used with an arbitrary number of structural order parameters. These terms are implemented into the phase field equation solver in ELK, which was developed by Tonks et al. [13]. The effect of hydrogen concentration on $F_{elastic}$ within the matrix is ignored, but it can be added as necessary. One material property class has been written to parameterize $f(\chi, \phi_1, \phi_2, \phi_3)$, κ_χ, κ_h, M, and L_h.

3.2 Solid mechanics and implementation

As the phase field formulation couples elastic strain energy into the model, it is necessary to solve for mechanical equilibrium described by

$$\nabla \cdot \sigma = 0, \tag{6}$$

where σ is the stress field tensor. Eq. 6 is written in the variational form as

$$\int_V \psi\left(\nabla \cdot \sigma\right) dV = -\int_V \nabla\psi \cdot \sigma dV + \int_S \psi\sigma \cdot \mathbf{n} dS = 0, \tag{7}$$

where ψ is the test function and $\mathbf{n}$ is the unit surface normal. In the linear elastic regime, the stress is related to the displacement field as

$$\sigma_{ij} = C_{ijkl} \cdot \frac{1}{2}\left(\frac{du_i}{dx_j} + \frac{du_j}{dx_i}\right) \tag{8}$$

where $\mathbf{u} = (u_1, u_2, u_3)$ is the displacement field. Eq. 7 is solved for displacement fields using the Tensor Mechanics system, a full tensor math suite of classes that we developed and contributed to in ELK, which handles any anisotropic elasticity. In addition, one material property class has been written for Hyrax that calculates local strains ($\tilde{\epsilon}_{ij}$) and elastic strains ($\tilde{\epsilon}_{ij} - \epsilon_{ij}^{0h}$) for an arbitrary number of orientation variants.

3.3 Explicit nucleation algorithm and implementation

The incorporation of an explicit nucleation algorithm using classical nucleation theory into a phase field model was pioneered by Simmons [2]. Using this method, the nucleation rate for critical nuclei, J^*, is calculated within Hyrax for each element in the phase field simulation,

$$J^* = ZN\beta^* \exp\left(\frac{-\Delta G^*}{k_B T}\right) \exp\left(\frac{-\tau}{t}\right) \tag{9}$$

where Z is the Zeldovich non-equilibrium correction factor, N is the number of atoms within the element, β^* is the rate at which an atom joins a critical nucleus, making it a supercritical nucleus, T is the temperature, k_B is Boltzmann's constant, τ is the incubation time, t is the time, and ΔG^* is the critical nucleus activation energy [14]. The activation energy contains any salient effects, such as elastic strain energy or concentration dependence. In Hyrax, ΔG^* is calculated for a spherical nucleus as [15, 16]

$$\Delta G^* = \frac{\alpha \gamma^d}{\Delta f^{d-1}} \tag{10}$$

where α is a geometrical factor that depends on the dimensionality of the problem, γ is the interfacial energy, and d is the dimension. In addition, Δf is the difference between the free energies of the precipitate and matrix phases, which includes the chemical free energy, self-elastic energy and elastic interaction energy of the nucleus with the existing microstructure. This is given very generally as

$$\Delta f\left(\chi\left(\mathbf{r}\right), \phi\left(\mathbf{r}\right), \sigma_{ij}\left(\mathbf{r}\right)\right) = f\left(\chi_m, \phi_m, \sigma_{ij}\left(\mathbf{r}\right)\right) - f\left(\chi_p, \phi_p, \sigma_{ij}\left(\mathbf{r}\right)\right)$$

$$+\frac{\partial f}{\partial \chi}|_{\chi_m}\left(\chi_m - \chi_p\right) + \frac{\partial f}{\partial \phi}|_{\phi_m}\left(\phi_m - \phi_p\right), \tag{11}$$

where m and p indicate the equilibrium value of the field variable in the matrix and precipitate phases, respectively. It is assumed that the nucleus attains the values of ϕ and χ corresponding to the equilibrium values for the precipitate phase. More specifically,

$$\Delta f\left(\chi\left(\mathbf{r}\right), \phi\left(\mathbf{r}\right), \sigma_{ij}\left(\mathbf{r}\right)\right) = \Big[f\left(\chi_m, \phi_m\right) + \frac{1}{2} C_{ijkl} \epsilon^0_{ij}\left(\chi_m, \phi_m\right) \epsilon^0_{kl}\left(\chi_m, \phi_m\right)$$

$$-C_{ijkl}\tilde{\epsilon}_{ij}\left(\mathbf{r}\right) \epsilon^0_{kl}\left(\chi_m, \phi_m\right)\Big] - \Big[f\left(\chi_p, \phi_p\right) + \frac{1}{2} C_{ijkl} \epsilon^0_{ij}\left(\chi_p, \phi_p\right) \epsilon^0_{kl}\left(\chi_p, \phi_p\right)$$

$$-C_{ijkl}\tilde{\epsilon}_{ij}\left(\mathbf{r}\right) \epsilon^0_{kl}\left(\chi_p, \phi_p\right)\Big] + \frac{\partial f}{\partial \chi}|_{\chi_m, \phi_m}\left(\chi_m - \chi_p\right) + \frac{\partial f}{\partial \phi}|_{\phi_m, \chi_m}\left(\phi_m - \phi_p\right) \tag{12}$$

$$\frac{\partial f}{\partial \chi}|_{\chi_m,\phi_m} = \left\{ \frac{\partial f}{\partial \chi} + C_{ijkl} \frac{\partial \epsilon^0_{ij}\left(\chi\left(\mathbf{r}\right),\phi\left(\mathbf{r}\right)\right)}{\partial \chi} \epsilon^0_{kl}\left(\chi\left(\mathbf{r}\right),\phi\left(\mathbf{r}\right)\right) - \frac{1}{2} C_{ijkl} \frac{\partial \epsilon^0_{ij}\left(\chi\left(\mathbf{r}\right),\phi\left(\mathbf{r}\right)\right)}{\partial \chi} \tilde{\epsilon}_{kl}\left(\mathbf{r}\right) \right\}|_{\chi_m,\phi_m} \quad (13)$$

$$\frac{\partial f}{\partial \phi}|_{\phi_m,\chi_m} = \left\{ \frac{\partial f}{\partial \phi} + C_{ijkl} \frac{\partial \epsilon^0_{ij}\left(\chi\left(\mathbf{r}\right),\phi\left(\mathbf{r}\right)\right)}{\partial \phi} \epsilon^0_{kl}\left(\chi\left(\mathbf{r}\right),\phi\left(\mathbf{r}\right)\right) - \frac{1}{2} C_{ijkl} \frac{\partial \epsilon^0_{ij}\left(\chi\left(\mathbf{r}\right),\phi\left(\mathbf{r}\right)\right)}{\partial \phi} \tilde{\epsilon}_{kl}\left(\mathbf{r}\right) \right\}|_{\phi_m,\chi_m} \quad (14)$$

Inserting Eqs. 13 and 14 into Eq. 12 gives the full equation solved by Hyrax to obtain the Δf term in Eq. 10. Finally, the nucleation probability, P, for each element is calculated every time step within Hyrax using [2]

$$P = 1 - \exp\left(-J^* \Delta t\right) \quad (15)$$

where Δt is the current simulation time step size. If the element contains a second-phase particle, the probability is assigned to zero. Because there are three hydride orientation variants, the nucleation probabilities are calculated three times (once for each variant).

Once the nucleation probability field has been calculated, it is necessary to determine the locations where new nuclei are to be introduced. This is accomplished using a Bernoulli trial on the nucleation probability. A random number is calculated between zero and one, and if the number is smaller than the nucleation probability, nucleation is set to occur at that location. A list of nuclei locations are generated within a user object class. Next, the finite element mesh is refined if necessary to introduce small nuclei into a coarse mesh. This is accomplished by passing the list of nuclei locations to a marker class, which marks the necessary elements to refine. Elements are then refined according to this marker and any error estimators. Finally, nuclei are seeded accordingly by another user object class that modifies the solution vector of the order parameter field to introduce nuclei as appropriate.

3.4 Boundary conditions, initial conditions, and post-processing

Various boundary conditions and initial conditions are available in MOOSE for use with Hyrax, including Dirichlet and Neumann boundary conditions. For example, a hydrogen concentration or a hydrogen flux can be specified, or fixed mechanical displacements or applied stresses can be specified. Typically, no-flux boundary conditions, $\nabla\phi_1 = \nabla\phi_2 = \nabla\phi_3 = 0$, are imposed at the computation domain boundaries for the structural order parameters. Finally, multiple postprocessors are available within MOOSE for extracting relevant data during the simulations. Useful postprocessors include integration of field variables (such as concentration, to determine the mass of the system), nodal maximum values of field variables, and the number counts of precipitates for each orientation variant, among others. Postprocessors can easily be added as necessary to provide "on-the-fly" data of essential information.

4 Order-parameter-only nucleation and verification

Significant effort has been made to verify the accuracy of the explicit nucleation algorithm employed within Hyrax (described in Sec. 3.3). To introduce nuclei into the phase field simulation, the value of the structural order parameter field (ϕ_1, ϕ_2 or ϕ_3) is altered at the nucleation site to the approximate equilibrium value for the second phase, while leaving the concentration field, χ, unchanged (termed "order-parameter-only nucleation"). The system is allowed to continue to evolve according to Eqs. 4 and 5, and solute diffuses into the nucleus region. The order parameter field in the new nucleus is fixed for several time steps to facilitate nucleation.

To verify that this algorithm captures classical nucleation behavior, validation studies were carried out against the Avrami equation [2, 3]. To this end, $\ln\left[\ln\left(1/\left(1-A(t)/A_f\right)\right)\right]$ is plotted against $\ln(t)$, where t is time, $A(t)$ is the area of the transformed phase, and A_f is the equilibrium area of the transformed phase. In two-dimensional, diffusion-controlled growth, a linear relationship of the form $y = mx + b$ results. The Avrami coefficient, m, for site saturation conditions (when all nuclei are present at the start of the simulation) is one, while the Avrami coefficient for concurrent nucleation and growth with a constant nucleation rate is two [3]. These studies were conducted with and without adaptive meshing to verify the mesh adaptivity portion of the code. Figure 2 illustrates a site saturation condition simulation and a concurrent nucleation and growth simulation. The agreements between the Avrami equation and the simulations demonstrate that order-parameter-only nucleation and its implementation within Hyrax accurately capture both site saturation and concurrent nucleation and growth behavior and are acceptable for further use.

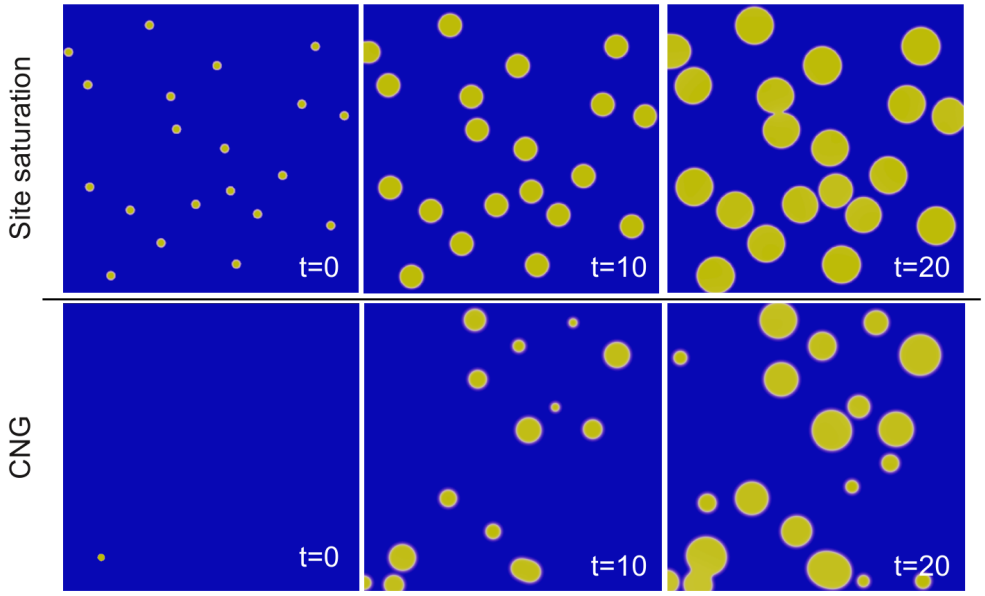

Figure 2: Structural order parameter field shown for two separate nucleation regimes, simulated using Hyrax. Top: site saturation conditions; all nuclei present at the initial condition of the simulation. Bottom: concurrent nucleation and growth (CNG) conditions; new particles and a large particle size distribution are observed.

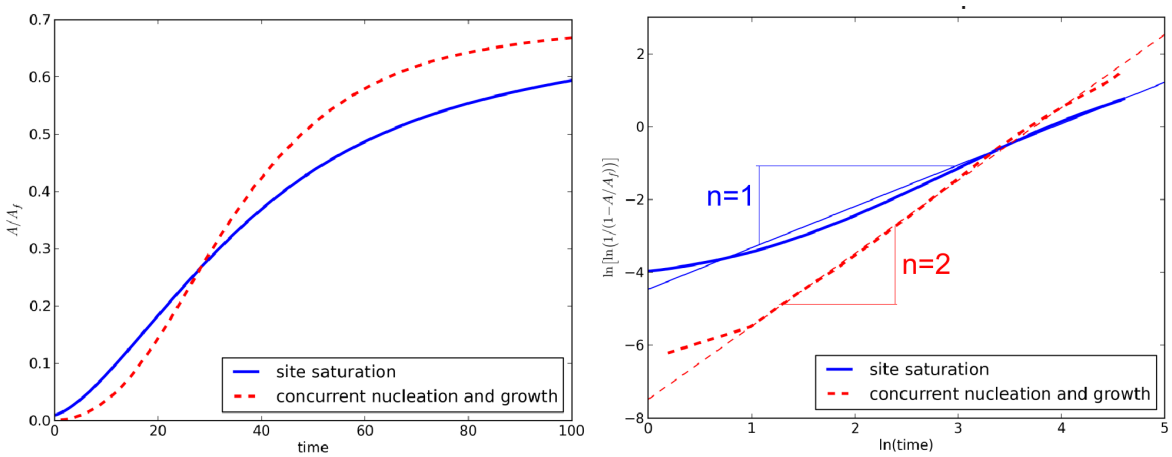

Figure 3: Left: The fraction of transformed phase for site saturation conditions and concurrent nucleation and growth conditions in 2D. Right: The Avrami plot of the transformation data.

5 Scaling study

A scaling study was performed on Fission, Idaho National Laboratory's largest distributed-memory cluster. It consists of 391 compute nodes, each with four 8-core 2.4 GHz AMD Opteron (6136) processors and 64GB of shared memory per node. A test problem was designed to be large enough to provide a sufficient workload for over five thousand processors; the details are provided in Table 1. The number of processors used to solve the problem were

recurrently reduced by half until the problem was too large to fit into memory. All of these runs were conducted using hybrid parallelism, i.e., MPI plus multithreading using Intel's Threaded Building Blocks. Six MPI processes per compute node were launched with five threads for each MPI process. Using hybrid parallelism drastically reduces communication overhead and improves the efficiency of the simulations.

Table 1: Problem size information for the Hyrax scaling study on Fission.

Simulation parameter	Number
Nodes	1,367,631
Elements	1,331,000
Degrees of freedom, physics system	19,146,834
Degrees of freedom, auxiliary system	27,951,000

Results from the scaling study are shown in Fig. 4 for the compute times for Hyrax's Jacobian and residual calculations. It can be seen that these computationally intensive portions of the Hyrax code scale efficiently across thousands of processors.

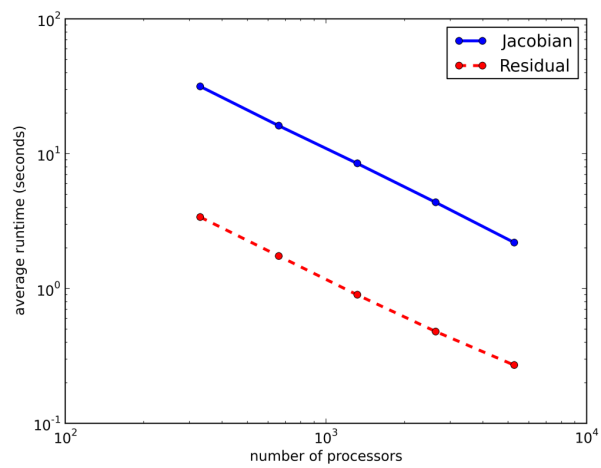

Figure 4: Average runtime versus number of processors for Hyrax Jacobian and residual calculations.

6 Examples

6.1 Stress fields calculations

Several examples are discussed below to illustrate several types of simulation results from Hyrax. Figure 5 shows the stress fields in the basal plane of hcp zirconium surrounding individual δ-hydride and γ-hydride particles. While δ-hydrides have the same misfit in the a and b directions (in the basal plane) and a different misfit in the c direction, resulting in platelet-shaped precipitates, γ-hydrides have different misfit in the a, b, and c directions,

leading to needle-shaped precipitates. The symmetry differences in the long-range stress fields induced by δ- versus γ-hydrides is clearly seen in Fig. 5; such differences could have significant impact on the subsequent precipitation and growth of hydrides within zirconium.

6.2 Evolution of hydride microstructure

Figure 6 illustrates an example of zirconium and γ-hydride microstructure evolution, with an earlier snapshot at $t = 6$ s in the left column, an intermediate snapshot at $t = 9$ s in the middle column, and a later snapshot at $t = 11.7$ s in the right column. The top row shows the hydrogen concentration field. The three hydride orientation variants, which tend to elongate along corresponding characteristic directions, are visible, particularly larger particles in Figs. 6b and 6c. Nuclei forming via the order-parameter-only nucleation algorithm (detailed in Section 4) can also be seen in Fig. 6a, b, and c. Depletion of hydrogen is particularly large around newly formed precipitates as a result of the nucleation algorithm, but it quickly attains equilibrium distribution around the precipitates. The middle row of Fig. 6 shows the σ_{22} stress field. The other stress fields (σ_{11} and σ_{12}, in 2D) are also available for visualization and analysis, but are not shown here. It can be seen that σ_{22} becomes increasingly complex with the formation of new precipitates; the evolution of σ_{11} and σ_{12} are similar. Finally, the bottom row of Fig. 6 shows the critical nucleus activation energy, ΔG^* (Eq. 10 with Eq. 12 for the Δf term), for the first hydride orientation variant. It is evident that ΔG^* varies significantly over the microstructure. Different variants have different values of ΔG^* for a given position due to the elastic contribution, thus allowing preferred nucleation of a certain variant. Addition fields, such as individual structural order parameter fields (ϕ_1, ϕ_2, and ϕ_3), nucleation rates, and nucleation probabilities for each hydride orientation variant, are computed and available for analysis in Hyrax.

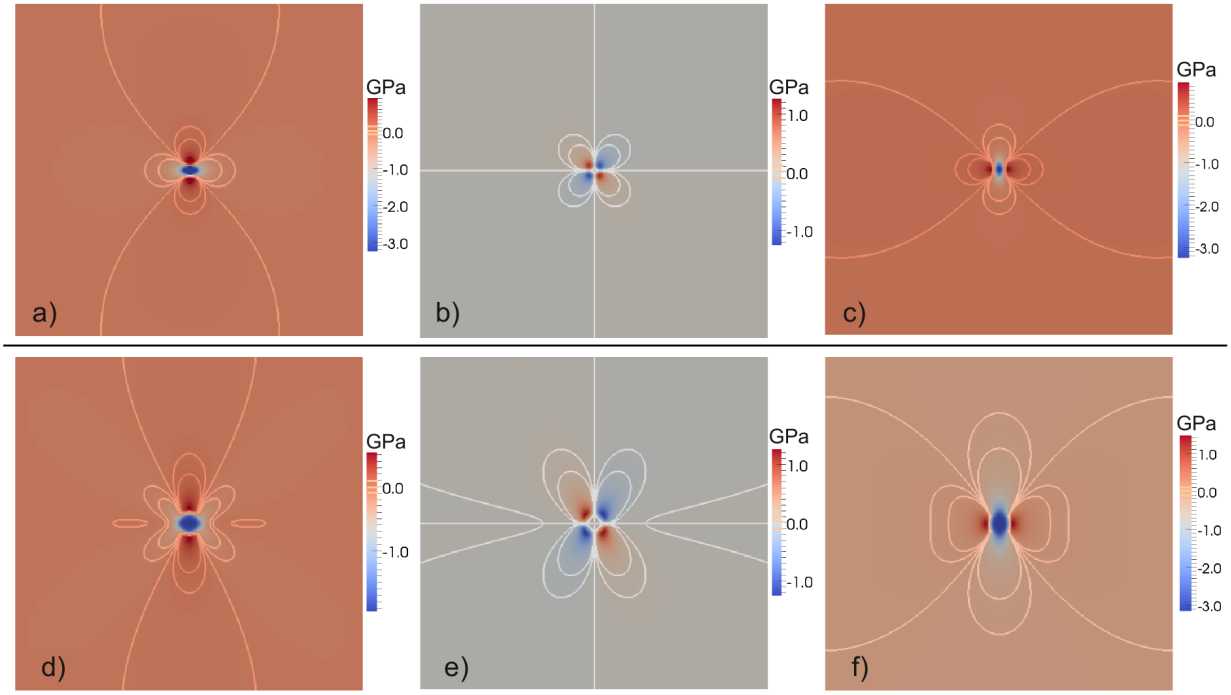

Figure 5: Stress fields in the basal hcp plane due to the presence of of a single δ-hydride a)-c) or γ-hydride d)-f). The subfigures a) and d) are σ_{11}; b) and e) are σ_{12}; c) and f) are σ_{22}. All contours are at 0, ± 50, and $\pm$ 100 MPa. The differences in stress field symmetries due to the different misfit strains are evident. A portion of the computational domain is shown.

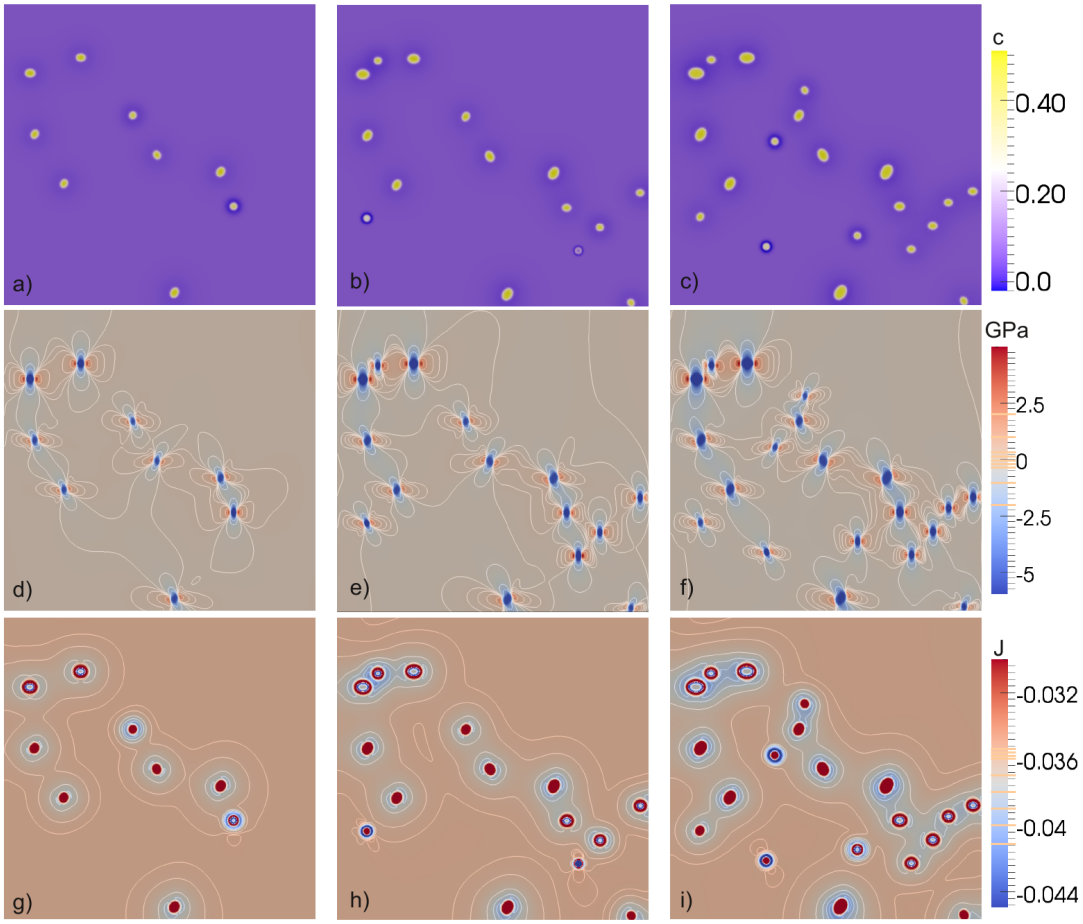

Figure 6: Example evolution of an hcp-zirconium and γ-hydride system, with three successive times ($t = 6$ s, $t = 9$ s, and $t = 11.7$ s) shown left to right. The subfigures are a)-c) concentration field; d)-f) σ_{22} field; g)-i) the activation energy, $\Delta G^* = \frac{\alpha\gamma^d}{\Delta f^{d-1}}$, for the first hydride orientation variant.

7 Future work

Hyrax development is continuing and will lead to several additional features in the near future. First is a free energy functional for zirconium and zirconium δ-hydrides. Work is currently underway to create a functional using data from Ref. [17], which is for the titanium-hydrogen system, a good surrogate for the zirconium-hydrogen system, and from zirconium-hydrogen phase diagram information [10, 18]. In addition, temperature evolution will be governed by the heat equation as

$$\frac{\partial T}{\partial t} = \nabla \cdot \kappa \nabla T = 0 \tag{16}$$

where T is the temperature, t is the time, and κ is the thermal conductivity. The calculated temperature will then be incorporated into the temperature dependence of the model parameters, such as the free energy functional, hydrogen mobility, and misfit strains. Upon

the incorporation of temperature dependence, Hyrax will fully describe the phenomena observed in the zirconium and δ-hydride system, such as terminal solid solubility hysteresis of hydrogen and macroscopic hydride reorientation.

8 Summary

The absorption of hydrogen into the cladding causes significant cladding microstructure and mechanical property changes due to the formation of zirconium hydride precipitates. In this report, the details of a phase field model of the microstructural evolution of the zirconium-hydrogen system were presented. In this model, the zirconium and zirconium are described using a hydrogen concentration and three structural order parameters, with concentration evolution governed by the Cahn-Hilliard equation and structural-order-parameter evolution governed by the Allen-Cahn equation. As the phase field formulation couples elastic strain energy into the model, it is necessary to solve for mechanical equilibrium, where linear elasticity is assumed. Classical nucleation theory is used to model the nucleation behavior of hydride precipitates, and an order-parameter-only nucleation algorithm for the introduction of nuclei into simulations was developed and verified. This report also discusses the implementation of the model into the Hyrax application, and scaling-study results demonstrate efficient scaling to over 5000 processors. Two examples were given to illustrate the modeling capabilities of Hyrax, including a comparison of the stress fields induced by the presence of δ- and γ-hydrides and progressive comparisons of hydrogen concentration, σ_{22} stress field, and ΔG^* values for a zirconium and γ-hydride microstructure. Finally, additional work needed to enhance Hyrax's prediction capabilities for δ-hydrides are discussed, namely, the parameterization of a zirconium and δ-hydride free energy functional and the introduction of temperature dependence into the model.

References

[1] D. Gaston, C. Newman, G. Hansen, D. Lebrun-Grandié, "MOOSE: A parallel computational framework for coupled systems of nonlinear equations," Nuclear Engineering and Design 239 (2009) 1768-1778.

[2] J. P. Simmons, C. Shen, Y. Wang, "Phase field modeling of simultaneous nucleation and growth by explicitly incorporating nucleation events," Scripta Materialia 43 (2000) 935-942.

[3] J. W. Christian, *The Theory of Phase Transformations in Metals and Alloys: Part I*, 2nd ed., Pergamon Press, New York (1975).

[4] A. G. Khachaturyan, *Theory of Structural Transformations in Solids*, Wiley, New York, 1983.

[5] R. N. Singh, P. Stahle, A. R. Massih, A. A. Shmakov, "Temperature dependence of misfit strains of delta hydrides of zirconium," Journal of Alloys and Compounds 436 (2007) 150-154.

[6] V. Perovic, G. R. Purdy, L. M. Brown, "Autocatalytic nucleation and elastic stabilization of linear arrays of plate-shaped precipitates," Acta Metallurgica 29 (1981) 889-902.

[7] V. Perovic, G. C. Weatherly, C. J. Simpson, "The role of elastic strains in the formation of stacks of hydride precipitates in zirconium alloys," Scripta Metallurgica 16 (1982) 409-412.

[8] V. Perovic, G. R. Purdy, "The role of shear transformation strains in the formation of linear arrays of precipitates," Scripta Metallurgica 15 (1981) 217-221.

[9] V. Perovic, G. R. Purdy, "Autocatalytic nucleation and elastic stabilization of linear arrays of plate-shaped precipitates," Acta Metallurgica 29 (1981) 889-902.

[10] A. McMinn, E. C. Darby, J.S. Schofield, "The terminal solid solubility of hydrogen in zirconium alloys," Zirconium in the Nuclear Industry: Twelfth International Symposium, ASTM STP 1354, G.P. Sabol and G.D. Moan, Eds., American Society for Testing and Materials, West Conshohocken, PA, 2000, pp. 173-195.

[11] B. S. Kirk, J. W. Peterson, R. H. Stogner, G. F. Carey, "libMesh: a C++ library for parallel adaptive mesh refinement/coarsening simulations," Engineering with Computers 22 (2006) 237-254.

[12] X. H. Guo, S. Q. Shi, Q. M. Zhang, X. Q. Ma, "An elastoplastic phase-field model for the evolution of hydride precipitation in zirconium. Part I: Smooth specimen," Journal of Nuclear Materials 378 (2008) 110–119.

[13] M. R. Tonks, D. Gaston, P. C. Millet, D. Anders, P. Talbot, "An object-oriented finite element framework for multiphysics phase field simulations," Computational Materials Science 51 (2012) 20-29.

[14] R. W. Balluffi, S. M. Allen, W. C. Carter, *Kinetics of Materials*, Wiley-Interscience, Hoboken, New Jersey, 2005.

[15] C. Shen, J. P. Simmons, Y. Wang, "Effect of elastic interaction on nucleation: I. Calculation of the strain energy of nucleus formation in an elastically anisotropic crystal of arbitrary microstructure," Acta Materialia 54 (2006) 5617-5630.

[16] C. Shen, J. P. Simmons, Y. Wang, "Effect of elastic interaction on nucleation: II. Implementation of strain energy of nucleus formation in the phase field model," Acta Materialia 55 (2007) 1457-1466.

[17] Q. Xu, A. Van der Ven, "First-principles investigation of metal-hydride phase stability: the Ti-H system," Physical Review B 76 (2007) 064207.

[18] E. Zuzek, J. P. Abriata, A. San-Martin, F.D. Manchester, "The H-Zr (Hydrogen-Zirconium) System," Bulletin of Alloy Phase Diagrams 11 (1990) 385-395.